Accepted Manuscript

Strengthening mechanisms of graphene sheets in aluminium matrix nanocomposites

A. Fadavi Boostani, S. Yazdani, R. Taherzadeh Mousavian, S. Tahamtan, R. Azari Khosroshahi, D. Wei, D. Brabazon, J.Z. Xu, X.M. Zhang, Z.Y. Jiang

PII: S0264-1275(15)30473-1
DOI: doi: 10.1016/j.matdes.2015.09.063
Reference: JMADE 633

To appear in:

Received date: 27 May 2015
Revised date: 10 September 2015
Accepted date: 11 September 2015

Please cite this article as: A. Fadavi Boostani, S. Yazdani, R. Taherzadeh Mousavian, S. Tahamtan, R. Azari Khosroshahi, D. Wei, D. Brabazon, J.Z. Xu, X.M. Zhang, Z.Y. Jiang, Strengthening mechanisms of graphene sheets in aluminium matrix nanocomposites, (2015), doi: 10.1016/j.matdes.2015.09.063

Strengthening mechanisms of graphene sheets in aluminium matrix nanocomposites

A. Fadavi Boostani[a], S. Yazdani[b], R. Taherzadeh Mousavian[b], S. Tahamtan[c], R. Azari Khosroshahi[b], D. Wei[d], D. Brabazon[e], J.Z. Xu[c], X.M. Zhang[c], Z.Y. Jiang[*a]

[a] School of Mechanical, Materials and Mechatronic Engineering, University of Wollongong, NSW 2522, Australia

[b] Faculty of Materials Engineering, Sahand University of Technology, Tabriz, Iran

[C] State Key Laboratory of Rolling and Automation, Northeastern University, Shenyang, Liaoning 110004, China

[d] School of Electrical, Mechanical and Mechatronic Systems, University of Technology, Sydney, NSW 2007, Australia

[e] Advanced Processing Technology Research Centre, School of Mechanical & Manufacturing Engineering, Dublin City University, Dublin, 9, Ireland

Abstract

Uniform dispersion of SiC nanoparticles with a high propensity to agglomerate within a thixoformed aluminium matrix was attained using a graphene encapsulating approach. The analytical model devised in this study has demonstrated the significant role of shear lag and thermally activated dislocation mechanisms in strengthening aluminium metal matrix composites due to the exceptional negative thermal expansion coefficient of graphene sheets. This, in turn, triggers the pinning capacity of nano-sized rod-liked aluminium carbide, prompting strong interface bonding for SiC nanoparticles with the matrix, thereby enhancing tensile elongation.

Keywords: Metal matrix composites; Graphene sheets; Strengthening mechanisms, Fracture; Ductility

1- Introduction

Metal matrix nano-composites (MMNCs) strengthened with ceramic nanoparticles outperform the disadvantages associated with the conventional metal matrix composites (MMCs) because of the enhanced mechanical and electrical properties and the diminished coefficient of thermal expansion and friction [1]. This makes MMNCs an appropriate candidate to be employed in advanced industries such as automobile, aerospace and thermal management [1, 2].

∗Corresponding author. Tel.:+61 02 42214545.
E-mail addresses: jiang@uow.edu.au (Z.Y. Jiang), afb496@uowmail.edu.au (A. Fadavi Boostani)

Enhancing the tensile elongation of aluminium metal matrix composites (AMMCs) reinforced with ceramic nanoparticles, however, is a challenging task via both solid and liquid processing routes. This is attributed to the large surface-to-volume ratio and poor wettability, prompting a high degree of particulate agglomeration and imperfect interface bonding of these nanoparticles with the surrounding matrix, respectively [3, 4].

Different methods have been suggested to overcome this problem, including semi-solid stirring[5] and ball milling with ultrasonic treatment [6] but they have not been very successful. This is attributed to the fact that they have mainly concentrated on the deagglomeration of nanoparticles when they are mixing with the metallic alloy during the manufacturing process rather than in their as-received state, diminishing the efficiency of the process due to the lower wettability of these nanoparticles with most metal matrices [5, 7, 8]. Most importantly, these studies suffer from exploiting thermal models to predict the interaction of the nanoparticles with the solid/liquid interface during solidification.

Thixoforming is defined as a two-step process encompassing the preparation of a feed stock material with a thixotropic characteristic, followed by reheating the feed stock material to a semi-solid temperature in order to provide the semi-solid slurry which is then subjected to the deformation process [9-11]. This process, unlike the preceding ones, is better able to alleviate the agglomeration of the nanoparticles due to the lower mobility of these particles within the highly viscous metallic matrix during the manufacturing process, but this process by itself is still immature to effectively deagglomerate nanoparticles.

It has been reported that graphene sheets possess the unique feature of having a two-dimensional shell(s) which can nucleate and anchor nano-particles on the edges and surface [12, 13]. Authors have shown [14] that graphene nanosheets (GNSs) can confer on nanoparticles the unique capacity to resist being repelled by the advancing solid/liquid interface during solid and liquid processing

routes. The ability of graphene sheets to alleviate the agglomeration of nano-particles during solid and liquid processing for the production of meal matrix composites, however, has hitherto not been reported.

Apart from this promising feature, to date, the actual enhancement in the thermal conductivity of SiC nanoparticles wrapped by graphene sheets and the strengthening mechanisms of graphene sheets are not well understood. This study, therefore, aims to investigate how the strengthening mechanisms of Orowan, Hall-Petch, shear lag and thermal enhanced dislocation relate to graphene reinforced AMMCs. To reach a more reliable strengthening model the thixoforming process, including forming an alloy in a semi-solid region with thixotropic behaviour, was utilized to diminish the detrimental effects of porosity associated with as-cast samples.

2- Materials and Methods

In order to prepare composite powder, i.e. preform, used for the fabrication of A357 thixoformed samples, a powder metallurgy process was utilized. This was conducted using a mixture containing SiC nanoparticles (45 nm, supplied by Nanostructured & Amorphous Materials, Inc.), graphene nanosheets (GNSs) with the average lateral size of 550 nm (supplied by Graphene Supermarket) as reinforcements and high purity aluminium powder (45 μm, supplied by Alpha Aesar Company with 99.5 % purity).

A Fritsch Pulverisette P5 planetary machine was used for ball milling without interruption under high purity (99.999%) argon gas in a liquid nitrogen environment (cryomilling) added constantly to compensate for evaporation. The stainless steel vial was sealed with an elastomeric O ring. The stainless steel balls to powder weight ratio was 15:1, and the rotation rate of the vial was 250 rpm under a total milling time of 2h. The amount of GNSs and SiC nanoparticles was adjusted to 83 Wt. % SiC and 17 Wt. % graphene. These components were milled for 0.5h without aluminium powder. Subsequently, the milling was continued for 1.5h by adding aluminium powder to the mixture

containing graphene and SiC, by setting the aluminium weight equal to 45Wt. % of the total SiC and graphene powders, in order to enhance the incorporation of the SiC nanoparticles into the molten aluminium. The prepared powder was then injected into molten A357 aluminium alloy in an atmosphere controlled with high purity (99.999%) argon gas (6 lit/min) in the semi-solid state. Table 1 demonstrates the chemical composition of the A357 alloy used in this study.

Table1. Chemical composition of A357 alloy used in this study (Wt. %)

Al	Si	Fe	Cu	Mn	Mg	Zn	Ti
Bal.	7.0	<0.2	<0.2	<0.1	<0.3	<0.1	<0.2

SiC nanoparticles with two different processing histories were used including (i) as received SiC nanoparticles and (ii) SiC nanoparticles encapsulated by graphene sheets (prepared, as noted above, by the milling process). After the entire alloy in the crucible was melted, it was cooled to 605°C and held at this temperature with a solid fraction of about 0.30 [15]. The stirring process was conducted on the semi-solid alloy (using a graphite impeller) at 400 rpm associated with uniform adding of prepared powders over a time period of approximately 5 min associated with adding 1Wt. % Mg as a wetting agent. A non-contact ultrasonic process was then implemented during casting using an ultrasonic chamber (Bandelin-Germany Make – Model: RK – 100H), which can vibrate at a frequency of 35 kHz. After the completion of particle feeding, mixing was continued for an extra 1 minute. Finally, the composite slurry was poured into a pre-heated cast iron mould using a bottom-pouring system to prepare the semi-solid billet. The thixoforming process was conducted on the prepared billets based on the procedure described by S. Kandemir at a fabrication temperature of 580 $^{\circ}$C, i.e. $T_{Fabrication}$, with continuous application of thixoforming pressure to room temperature, i.e. T_{test}=25 $^{\circ}$C [16]. Table 2 represents a nomination system used to identify different specimens in the rest of this paper.

Table 2: Nomination system of the specimens

Name used in the paper	Different treatment applied on samples		
	Thixoforming	Graphene	Incorporation of SiC
A357	-	-	-
Thix	*	-	*
GThix	*	*	*

The density of the samples was measured by the Archimedes method for at least three different samples in order to calculate the porosity of the samples. TEM analysis was performed using a Philips CM200 at an accelerating voltage of 200 kV. Fractographic investigations were conducted using field emission scanning electron microscopy (FE-SEM) performed in a JEOL JSM-7500FA. Tensile properties were measured using a Hounsfield universal test machine at a cross-head speed of 0.5 mms^{-1} for at least three samples in order to confirm the repeatability of the measurements.

3- Results and discussion

Fig. 1 demonstrates TEM images captured from the nanostructure of (a) Thix, (b) GThix and (c) the high magnification image of the GThix sample accompanied by the selected area diffraction (SAD) pattern of the rectangular area.

As shown by arrows in Fig. 1 (a), although SiC nanoparticles in the Thix sample are agglomerated at the grain boundaries, they are mostly engulfed within the grain interior in the GThix sample, as demonstrated in Fig. 1(b).

In Fig. 1(c), graphene sheets appear in the GThix sample with two different morphologies: onion like graphene shells (OLGS) and disk-shaped graphene sheets (DSGS). There is also some evidence for the formation of nano-sized rod-shaped aluminium carbide (NRAC) at the interface of the OLGS and the DSGS with the aluminium matrix, as shown by white arrows in Fig. 1(c). This has also been confirmed by the selected area diffraction (SAD) pattern of the rectangular region in Fig. 1(c) and high resolution TEM (HRTEM) picture as demonstrated in the bottom inset of Fig. 1(c).

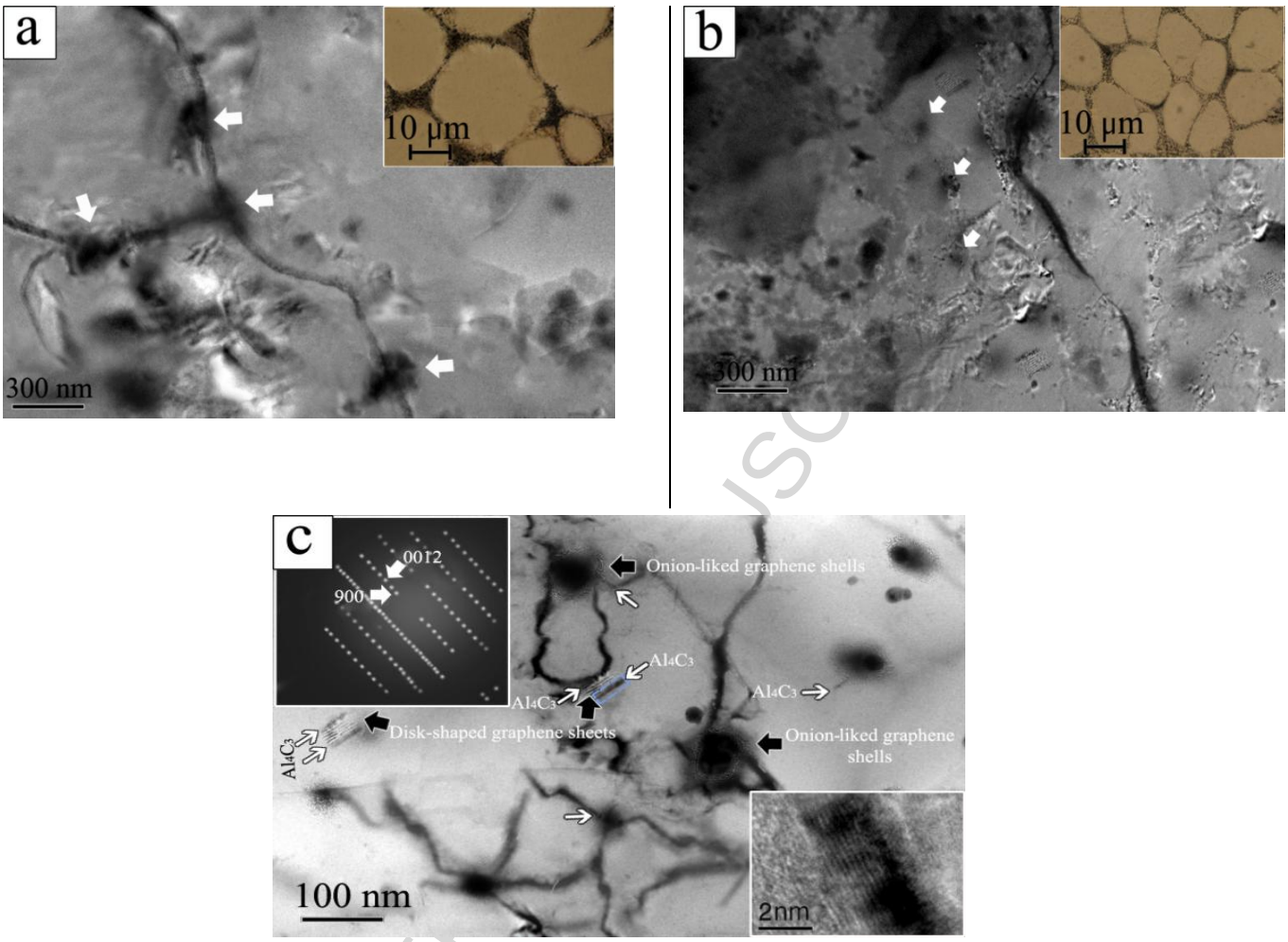

Fig. 1: TEM micrographs of (a) Thix sample, (b) GThix samples associated with corresponding optical images as insets and (c) the high magnification image of the GThix sample accompanied by the selected area diffraction (SAD) pattern of the rectangular area.

The white arrows demonstrate the location where the reaction for the formation of NRAC is started at the damaged regions of the graphene sheets. The formation of NRAC is known to occur between the aluminium and the defective regions of the graphene sheets and can be expressed by the following chemical reaction scheme:

$$4Al_{(l)} + 3C_{(s)} \rightarrow Al_4C_3 \quad (1)$$

There is, however, no evidence for the formation of NRAC in the Thix sample and this is attributed to the lower temperature (580 °C) used for manufacturing this sample. It has been reported that

without any external source of carbon, the reaction for the formation of Al_4C_3 can occur between SiC reinforcements and molten aluminium using the following reaction:

$$4Al_{(l)} + 3SiC_{(s)} \rightarrow Al_4C_3 + 3Si \quad (2)$$

The change in free energy (ΔG) for this reaction is given by the following equation [17]:

$$\Delta G(Jmol^{-1}) = 113900 - 12.06TlnT + 8.92 \times 10^{-3}T^2 + 7.53 \times 10^{-4}T^{-1} + 21.5T + 3RTln\,(a_{Si}) \quad (3)$$

where a_{Si} is the silicon chemical activity in molten aluminium, R the universal gas constant and T the absolute temperature (K). Eq. (3) registers a negative value for ΔG when the temperature exceeds 727 °C (1000 K) which is higher than the processing temperature of the Thix sample.

It has been asserted qualitatively that the SiC nanoparticles encapsulated by OLGS, as shown in Fig. 1(c), have a high tendency to be engulfed within the grain interior and this has been ascribed to the enhanced thermal conductivity of these particles [14].

The model presented in Eq. (4) predicts that particles with higher thermal conductivity are more prone to be engulfed within grains rather than being agglomerated at grain boundaries. The subscripts p and l refer to properties of the particles and the liquid, respectively.

$$\mathbf{K_P > K_l \ for\ engulfment} \quad (4)$$

The following model (Eq. (5)) was built based on heat diffusivity [18] characteristics using thermal conductivity (k), specific heat (c_p) and density (ρ):

$$\sqrt{\frac{K_P \cdot \rho_P \cdot C_P^P}{K_l \cdot \rho_l \cdot C_P^l}} > 1 \ \ for\ engulfment \quad (5)$$

The aforementioned model demonstrate that augmenting the thermal conductivity of particles results in increasing the possibility of their entrapment within grain boundaries due to the change of the interface shape from convex to concave [19-22].

It is also postulated that SiC nanoparticles encapsulated by graphene shells have higher thermal conductivity than the ones not wrapped by graphene shells [23, 24]. This is attributed to the fact that

the thermal conductivity of graphene shells on SiC nanoparticles is better conserved in bilayer and trilayer GNSs than in single layer GNSs [25].

The insets in Fig. 1 show the optical images of (a) Thix and (b) GThix samples, respectively. Image analysis results have shown a considerable reduction in the grain size of the GThix samples (D=14μm) compared with the Thix samples (D=30μm), substantiating the refining effect of well-dispersed SiC nanoparticles in the GThix sample rather than thixoforming pressure in the Thix sample. Fig. 2 shows the stress-strain curves of samples studied associated with schematic pictures representing their real microstructure. As can be seen from Fig. 2, the graphene encapsulating process has enhanced significantly the tensile properties of the PGT samples.

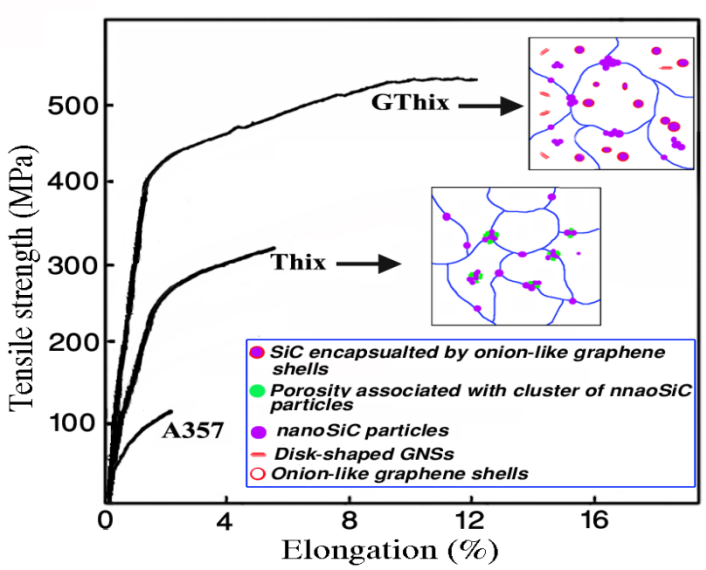

Fig.2. Stress-strain curve of A357, Thix and GThix samples accompanied with schematic illustration of their nanostructures.

Table 3 represents the tensile properties and porosity content of the samples resulting from the analysis of different samples. According to Table 3, the yield strength (σ_{YS}) and ultimate tensile strength (σ_{UTS}) of the GThix sample are considerably higher than the Thix sample by 81% and 60%, respectively, and this is ascribed to the uniform distribution of SiC nanoparticles and the lower porosity of this sample.

Table 3: The average values of yield stress (σ_{YS}), ultimate tensile strength (σ_{UTS}), total elongation (E %) and porosity content of samples

Samples	σ_{YS}	σ_{UTS}	Elongation (E %)	Porosity (%)
A357	75±2	125±3	2±0.3	3±0.1
Thix	221±7	326±10	5.4±0.3	0.9±0.2
GThix	401±11	523±13	12.1±0.5	0.5±0.2

±: Represents 95 pct. confidence interval.

Fig. 3(a) represents the cleavage fracture surface of the Thix sample which is attributed to the agglomeration of SiC nanoparticles in this sample, as shown by arrows.

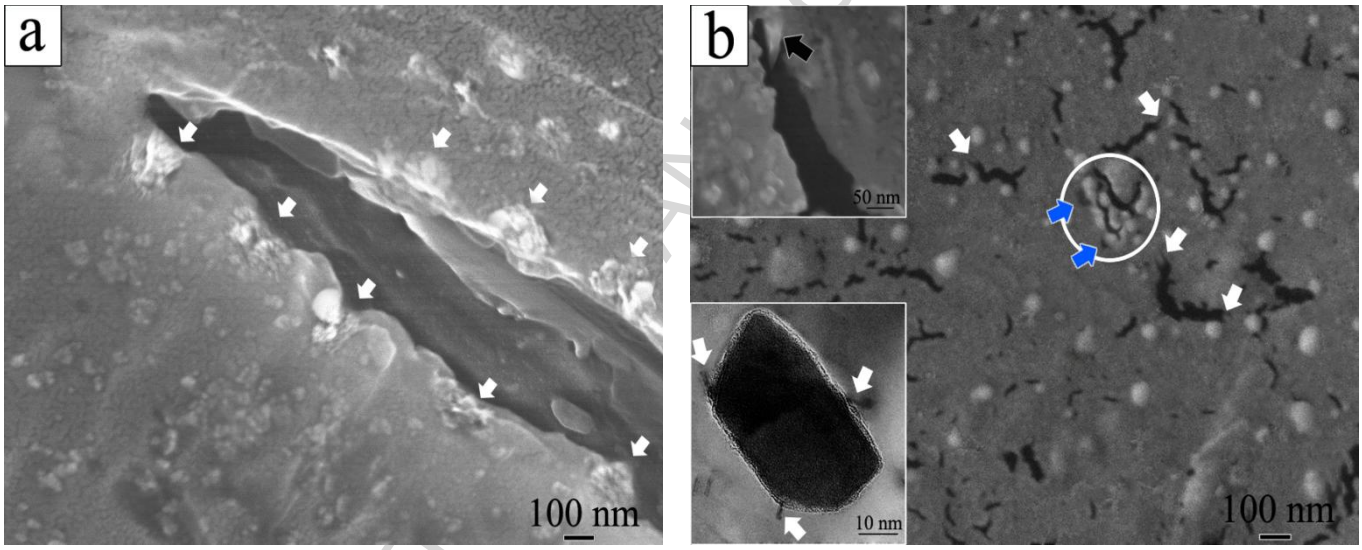

Fig. 3: Fracture side-view of (a) Thix and (b) GThix samples.

This agglomeration increases the probability of particle cracking associated with a higher crack propagation rate due to the settlement of these particle at the grain boundaries, thereby diminishing the ductility.

Fig. 3(b), in contrast, shows that well-dispersed SiC nanoparticles in the GThix sample are not prone to cracking or interfacial decohesion. The former is attributed to the lower possibility of cracking associated with nanoparticles and the latter can be attributed to the higher levels of plastic constraint exerted by the NRAC formed at the interface of OLGS and DSGS with aluminium, as shown by arrows in Fig. 1(c) and in the bottom inset of Fig.3 (b), respectively. The aforementioned plastic constraint is fortified by the expansion of OLGS and DSGS during solidification due to the

exceptional negative thermal expansion coefficient of graphene, thereby effectively prompting the mechanical bonding, i.e. pinning, of the SiC nanoparticles to the matrix.

These, in turn, trigger matrix cavitation through the aluminium matrix, postponed to higher strain fields, i.e. prolonged ductility. To have a better insight into the degree of strain imposed on the NRAC nucleated at the interface of SiC nanoparticles encapsulate by graphene sheets and an aluminium matrix, Eq. (6) was developed by J. F. Nye [26] to calculate the strain value exerted on the interface due to the mismatch between the thermal coefficient expansion between the graphene and surrounding aluminium matrix: :

$$\boldsymbol{\varepsilon^T = \int_{T_R}^{T_F} (\alpha_M - \alpha_G)\, dT \approx \Delta\alpha \Delta T} \quad (6)$$

Where T_F, T_R, ΔT, α_m and α_G represent the fabrication temperature (580°C), room temperature (25°C), difference between the fabrication temperature and room temperature, thermal expansion coefficient of matrix and graphene sheets, respectively. Table 4 lists the pertinent physical and mechanical properties of the composite constituents.

Table 4: physical and mechanical properties of materials [27-30].

Parameter	Unit	Al	SiC	Graphene
Burgers vector (b)	nm	0.25	—	Not fixed
Thermal expansion coefficient (α)	$\times 10^{-6}$/°C	21.4	4.3	-6
Shear modulus (G)	MPa	25	—	250
Young modulus (GPa)	GPa	70	427	1000
Poisson ratio	—	0.35	0.17	0.16
Taylor factor (M)	—	3	—	—

Having considered Eq. (6) using the values noted in Table 4, it is clear that SiC nanoparticles encapsulated by graphene sheets can impose more plastic strain on the NRAC, nucleated on the interface of graphene sheets and the aluminium matrix, compared to the SiC nanoparticles not wrapped by graphene sheets, thereby augmenting their pinning capacity.

The progressive propagation of cracks via the microvoid coalescence mechanism is also deflected and hindered by a fiber (graphene) pull-out mechanism activated by the DSGS, as shown by white

arrows in Fig. 3(b) and the top inset of Fig. 3(b). Some SiC nanoparticles in the GThix sample, however, are agglomerated with a high tendency to cracking, as shown by the white circle in Fig. 3(b), promoting cracking that can be blocked by the graphene pull-out mechanism.

This study aims at presenting a new analytical model (Eq. (7)) by incorporating a modified shear-lag model (continuum mechanics approach) and an enhanced dislocation density model (micromechanics strengthening approach) into the model proposed by Ramakrishnan [31], as the latter generally is used for micron-sized particles.

$$\boldsymbol{\sigma_y^{GThix} = \sigma_y^{Thix}\left(1+\omega_L^{DSGS}\right)(1+\omega_T)\left(1+\omega_{Orowan}^{DSGS}+\omega_{Orowan}^{OLGS}\right)+\sigma_y^{Hall-Petch}\left(\sigma_i+\frac{k}{\sqrt{D}}\right)} \quad (7)$$

Equation (7) takes into account the strengthening effects of graphene sheets, manifested in the form of load bearing (ω_l), thermal enhanced dislocation density (ω_T), and the Orowan (ω_{Orowan}), and Hall-Petch mechanisms, on the yield strength of the Thix sample (σ_y^{Thix}) in order to approximate the yield strength of the GThix sample (σ_y^{GThix}).

Regarding Hall-Petch strengthening, the σ_i , k and D define the intrinsic stress of the material (σ_i= 15.7 MPa) and k is the material constant (k = 0.068 MPa/M$^{0.5}$) for aluminium[32]. The Hall-Petch relationship has shown a 33.87 MPa enhancement in the yield strength of the GThix sample due to the refining effect of SiC nanoparticles encapsulated by graphene sheets. To have a subtle approximation of σ_y^{GThix}, it is crucial to determine strengthening contributors including ω_l, ω_T, ω_{Orowan}^{DSGS} and ω_{Orowan}^{OLGS} in Eq. (7).

It is generally agreed that the load transfer from the ductile matrix to the hard reinforcements (i.e. ceramic and graphene) under an applied external load contributes to the strengthening of the base material according to the modified shear lag model proposed by Nardone and Prewo [33]. To investigate the concept of load transfer from the composite matrix to the embedded DSGS and OLGS, the classical shear lag model [34] was used. For this reason the two-dimensional elastic

configuration was considered for a platelet of length L, thickness t and elastic modulus E, bonded to a matrix material of thickness λ.

The stress–strain relation along the axial direction of the platelet is $\sigma_f = E\varepsilon_f$, where $\sigma_f$denotes the axial stress and $\varepsilon_f$the axial strain in the platelet.The equilibrium of the forces along the length of the platelet is achieved using Eqs. (8) and (9).

$$\tau_p dx = -t d\sigma_f \tag{8}$$

$$\frac{\tau_p}{t} = -\frac{d\sigma_f}{dx} \tag{9}$$

It is supposed that the matrix surrounding the graphene platelet can be displaced (δ) in the z direction and the shear strain (γ) is calculated using following Eq. (10).

$$\gamma = \frac{d\delta}{dz} \tag{10}$$

Having considered the shear stress modulus of the matrix, Eq. (10) can be rewritten in the form of Eq. (11) under the assumption that the shear stress of the matrix is transferred to the graphene platelet ($\tau = \tau_p$) via the graphene/matrix interface, as long as this interfacial bonding is perfect, which seems reasonable because of the negative thermal expansion coefficient of the graphene, as shown in Table 2.

$$\frac{d\delta}{dz} = \frac{\tau_p}{G_m} \tag{11}$$

Where G_m represents the shear modulus of the matrix, i.e. aluminium. The integration of Eq. (11) using the boundary conditions of ($z = \frac{t}{2}\ at\ \delta = \delta_f$) and ($z = \frac{\lambda}{2}\ at\ \delta = \delta_\lambda$) results in Eq. (12).

$$\delta_\lambda - \delta_f = (\frac{\tau}{2G_m})(\lambda - t) \tag{12}$$

To approximate the strain of the graphene platelet and the surrounding matrix, displacements in Eq. (12) can be converted to strain by considering that $e_f = \frac{d\delta_f}{dx}$ and $e_m = \frac{d\delta_m}{dx}$. So, differentiating Eq. (12) with respect to x, using Eq. (9) and the noted strains ($e_f\ and\ e_m$), results in Eq. (13):

$$e_f - e_m = (\frac{t\lambda}{2G_m})(\frac{d^2\sigma_f}{dx^2}) \quad (13)$$

By considering that generally $\lambda \succ\succ t$ and multiplying Eq. (13) by E_f , Eq. (13) can be written in the form of Eq. (14):

$$\frac{d^2\sigma_f}{dx^2} = (\frac{n^2}{t^2})(\sigma_f - e_m E_f) \quad (14)$$

In this equation, n can be defined as $n = \sqrt{\frac{2\,G_m}{E_f}\,(\frac{t}{\lambda})}$. Then the general solution for this differential equation can be written as:

$$\sigma_f = E_f e_m + C\sinh\left(\frac{nx}{t}\right) + D\cosh(\frac{nx}{t}) \quad (15)$$

Using the boundary conditions that if $x = 0$, then $\sigma_f = E_f e_m$ and if $x = \pm\frac{L}{2}$, then $\sigma_f = 0$, the constants C and D for Eq. (15) are achieved. Hence, the final solution of Eq. (15) can give the stress distribution along the length of the graphene platelet as Eq. (16):

$$\sigma_f = E_f e_m \left[1 - \frac{\cosh(\frac{nx}{t})}{\cosh(\frac{nL}{2t})}\right] \quad (16)$$

Additionally using Eq. (16) the interfacial shear stress for the graphene platelet can be calculated according to Eq. (17):

$$\tau_P = nE_f e_m \left[\frac{sinh(\frac{nx}{t})}{cosh(\frac{nL}{2t})}\right] \quad (17)$$

Having considered the aspect ratio of the graphene plate **a**nd the matrix strain (em), let ($s = \frac{L}{t}$), Eq. (16) and (17) can be rewritten in the following forms [35]:

$$\boldsymbol{\sigma_f = E_f e_m \left[1 - \frac{cosh(ns\frac{x}{L})}{cosh(\frac{ns}{2})}\right]} \quad (18)$$

$$\boldsymbol{\tau_P = nE_f e_m \left[\frac{sinh(s\frac{x}{L})}{cosh(\frac{ns}{2})}\right]} \quad (19)$$

Therefore, the maximum load transfer from the matrix to the graphene platelet is attainable for the composite with the higher value of *ns*. To reach this, it is necessary to reduce the distance between the graphene platelets (λ) and simultaneously diminish their thickness, as thickness (t) affects the n with square root but it has an inverse relationship with S ($S=L/t$). At this stage, it is also necessary to introduce a new parameter to correlate the *ns* value of the graphene platelet with the load-bearing improvement factor ($\boldsymbol{\omega_l}$) affected mainly by the volume fraction of the reinforcements [31]. To find the $\boldsymbol{\omega_l}$ value, it is imperative to ascertain the inter-particle spacing, as a function of the total graphene volume fraction (V_{Gr}). Hence, the $\boldsymbol{\omega_l}$ parameter is defined as:

$$\boldsymbol{\omega_l} = \sqrt{\frac{2G_m L^2}{E_f \lambda_{eff} t}} \tag{20}$$

Where λ_{eff} is an effective inter-particle spacing between the graphene sheets within the matrix, and can be calculated using Eqs. (21) and (22) [36]:

$$\boldsymbol{\lambda_{eff}^{DSGS}} = \mathbf{0.931}\sqrt{\frac{0.306\pi dt}{V_{Gr}^{DSGS}}} - \frac{\pi d}{8} - \mathbf{1.061}t \tag{21}$$

Where d, t and V_{Gr}^{DSGS} is the length, thickness and volume fraction of DSGS, respectively, and is measured by image analysis of at least 20 HRTEM micrographs.

Putting the values of t=10 nm, λ_{eff}=427 nm (calculated by Eq. (21)) and the values provided in Table 2 into Eq. (20) results in ω_l=0.15 for DSGS.

It should be noted that the V_{Gr}^{DSGS} and V_{Gr}^{OLGS} have been set to 0.18% and 0.82% of the total volume of the graphene (V_{Gr}=0.01) added as a raw material, respectively, and is measured along with other microstructural features such as L and t using image analysis of at least 20 HRTEM micrographs. The aforementioned calculations represent the significant effect of OLGS on load transfer and the subsequent strengthening the aluminium matrix compared to DSGS due to the lower thickness and angled formation of the NRAC in the former, fortifying the pinning and thereby the load transfer from the matrix to the SiC nanoparticles.

According to Table 2, exceptional difference in the thermal expansion coefficient of graphene compared to aluminium can significantly strengthen the aluminium matrix by generating thermally induced dislocation, as shown in Fig. 1(c), reaffirmed by a high strengthening contributor (ω_T) calculated by Eq. (22) [37].

$$\boldsymbol{\omega_T = \frac{1.25\, G_m b}{\sigma_y^{Thix}} \sqrt{\frac{12\,(T_{Fabrication}-T_{test})(\alpha_m-\alpha_{Gr})V_{Gr}}{b d_{Gr}(1-V_{Gr})}}} \quad (22)$$

Eq. (22) can be solved based on the values presented in Table 2, V_{Gr} is the total volume fraction of the graphene encompassing the graphene sheets and the shells encapsulating the SiC nanoparticles (0.01), d_{Gr} is related to the average diameter of the graphene sheets and shells within the aluminium matrix (45 nm), and σ_y^{Thix} is the yield strength of the Thix sample (221 MPa), resulting in ω_T=0.14. To determine the strengthening contribution of DSGS and the OLGS under the Orowan strengthening mechanism, two different models can be utilised [36].

$$\omega_{Orowan}^{DSGS} = \frac{MGb}{2\pi\sqrt{1-\vartheta}\sigma_y^{Thix}} \left(\frac{1}{0.931\sqrt{\frac{0.306\pi dt}{V_{Gr}^{Disc}}-\frac{\pi d}{8}}-1.061t} \right) ln\frac{1.225t}{b} \quad (23)$$

$$\boldsymbol{\omega_{Orowan}^{OLGS} = \frac{MGb}{2\pi\sqrt{1-\vartheta}\sigma_y^{Thix}\left(\frac{0.779}{\sqrt{V_{Gr}^{Onion}}}-0.785\right)d} ln\frac{0.785\, d}{b}} \quad (24)$$

The investigation of Eq. (23) and (24) using the values provided in Table 2, V_{Gr}^{DSGS} (0.0018),V_{Gr}^{OLGS} (0.0082), d (45 nm) and t (10 nm) which are the average diameter and thickness of at least 60 DSGS and OLGS measured using HRTEM analysis, respectively, gives the values of 0.13 and 0.23 for ω_{Orowan}^{DSGS} and ω_{Orowan}^{OLGS}, respectively. It should be noted that V_{Gr}^{DSGS} (0.0018) and V_{Gr}^{OLGS} (0.0082) are the effective volume fractions of the DSGS and the OLGS calculated based on image analysis of 20 HRTEM micrographs, respectively. This shows the greater role of the OLGS as compared to the DSGS. This discrepancy is attributed mainly to the orientation in which the

DSGS interact with active slip planes during the deformation process. This can be ascribed to the fact that the DSGS are assumed to have a habit plane perpendicular to the slip plane of the aluminium (111) in Eq. (23). In practice, however, some DSGS lie on the slip plane of the aluminium matrix, resulting in lower interaction between the DSGS and dislocation gliding on the matrix slip plane.

Fig. 4 shows the strengthening contributor values corresponding to different strengthening mechanisms, as calculated in the preceding equations, demonstrating the major role of thermally activated dislocation mechanism in augmenting the yield strength compared to the other strengthening mechanisms. As shown in Fig. 4, OLGS are stronger in strengthening aluminium matrix compared to the DSGS, attributed to the circular morphologies of these graphene sheets, thereby increasing the density of dislocation more effectively compared to the DSGS.

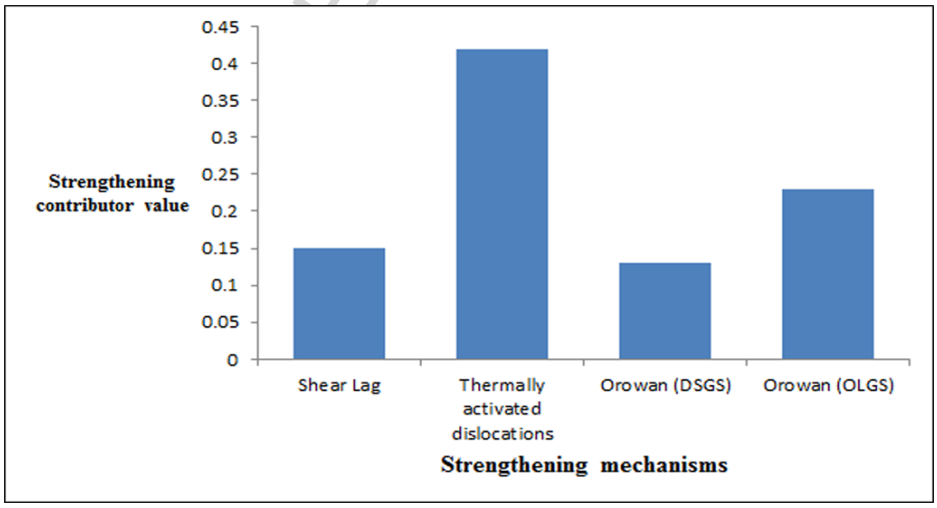

Fig. 4: Contribution of different strengthening mechanisms in enhancing the tensile yield strength of composite reinforced with graphene sheets.

By inserting the calculated values: $\omega_L^{DSGS} = 0.15$, $\omega_T = 0.42$, $\omega_{Orowan}^{DSGS} = 0.13$ and $\omega_{Orowan}^{OLGS} = 0.23$ into Eq. (7), σ_y^{GThix} is envisaged to be around 490 MPa, which is close to the value obtained experimentally (401 MPa). This suggests that the devised model is worth being considered to have a

subtle approximation about the effect of incorporation of graphene sheets in enhancing the tensile properties of the metal matrix composites. The difference between the tensile properties envisaged by the models and the experimental ones is attributed to four possible reasons including (i) the total volume fraction of the DSGS is assumed to have a habit plane perpendicular to the slip plane of the aluminium (111) in the model presented, however, some of them could settle on the slip plane of the aluminium matrix resulting in lower interaction between them and resulting in gliding dislocations; (ii) graphitization through Van der Waals interactions between some graphene sheets during the manufacturing process, resulting in the formation of unwrapped-graphene and hence agglomerated SiC nanoparticles; (iii) the possibility of overwrapping SiC nanoparticles by OLGS, as the calculation relies on the existence of at least 5 OLGS and (iv) high SiC nanoparticles content stimulates the incomplete graphene encapsulation process and in turn the agglomeration of these particles, thereby levelling off the strengthening.

4- Conclusion

This study reveals the major strengthening mechanisms coming to practice by implementation of graphene sheets as reinforcement in metal matrix composites. In fact, this study demonstrates that the graphene encapsulating process not only has a unique capacity to attenuate the agglomeration of SiC nanoparticles but also has the exceptional feature in strengthening the aluminium metal matrix composites using thermally activated dislocation and pinning the SiC nanoparticles to the matrix, thereby augmenting tensile ductility significantly.

Acknowledgments

The authors would like to acknowledge the use of facilities (ARC-LE0237478) within the University of Wollongong (UOW) Electron Microscopy Centre and especially the great assistance of Dr. Gilberto Casillas and Dr. Madeleine Strong Cincotta.

References

[1] Miracle D. Metal matrix composites – From science to technological significance. Composites Science and Technology. 2005;65:2526-40.

[2] Tjong SC. Recent progress in the development and properties of novel metal matrix nanocomposites reinforced with carbon nanotubes and graphene nanosheets. Materials Science and Engineering: R: Reports. 2013;74:281-350.

[3] El-Mahallawi I, Abdelkader H, Yousef L, Amer A, Mayer J, Schwedt A. Influence of Al2O3 nano-dispersions on microstructure features and mechanical properties of cast and T6 heat-treated Al Si hypoeutectic Alloys. Materials Science and Engineering: A. 2012;556:76-87.

[4] Naher S, Brabazon D, Looney L. Computational and experimental analysis of particulate distribution during Al–SiC MMC fabrication. Composites Part A: Applied Science and Manufacturing. 2007;38:719-29.

[5] Mohammadpour M, Khosroshahi RA, Mousavian RT, Brabazon D. A Novel Method for Incorporation of Micron-Sized SiC Particles into Molten Pure Aluminum Utilizing a Co Coating. Metall and Materi Trans B. 2015;46:12-9.

[6] Tahamtan S, Halvaee A, Emamy M, Jiang ZY, Fadavi Boostani A. Exploiting superior tensile properties of a novel network-structure AlA206 matrix composite by hybridizing micron-sized Al3Ti with Al2O3 nano particulates. Materials Science and Engineering: A. 2014;619:190-8.

[7] Beigi Khosroshahi N, Taherzadeh Mousavian R, Azari Khosroshahi R, Brabazon D. Mechanical properties of rolled A356 based composites reinforced by Cu-coated bimodal ceramic particles. Materials & Design. 2015;83:678-88.

[8] Beigi Khosroshahi N, Azari Khosroshahi R, Taherzadeh Mousavian R, Brabazon D. Effect of electroless coating parameters and ceramic particle size on fabrication of a uniform Ni–P coating on SiC particles. Ceramics International. 2014;40:12149-59.

[9] Fadavi Boostani A, Tahamtan S. Effect of a novel thixoforming process on the microstructure and fracture behavior of A356 aluminum alloy. Materials & Design. 2010;31:3769-76.

[10] Fadavi Boostani A, Tahamtan S. Fracture behavior of thixoformed A356 alloy produced by SIMA process. Journal of Alloys and Compounds. 2009;481:220-7.

[11] Fadavi Boostani A, Tahamtan S. Microstructure and mechanical properties of A356 thixoformed alloys in comparison with gravity cast ones using new criterion. Transactions of Nonferrous Metals Society of China. 2010;20:1608-14.

[12] Lightcap IV, Kosel TH, Kamat PV. Anchoring Semiconductor and Metal Nanoparticles on a Two-Dimensional Catalyst Mat. Storing and Shuttling Electrons with Reduced Graphene Oxide. Nano Letters. 2010;10:577-83.

[13] Pham VH, Dang TT, Hur SH, Kim EJ, Chung JS. Highly Conductive Poly(methyl methacrylate) (PMMA)-Reduced Graphene Oxide Composite Prepared by Self-Assembly of PMMA Latex and Graphene Oxide through Electrostatic Interaction. ACS Applied Materials & Interfaces. 2012;4:2630-6.

[14] Fadavi Boostani A, Tahamtan S, Jiang ZY, Wei D, Yazdani S, Azari Khosroshahi R, et al. Enhanced tensile properties of aluminium matrix composites reinforced with graphene encapsulated SiC nanoparticles. Composites Part A: Applied Science and Manufacturing. 2015;68:155-63.

[15] Naher S, Brabazon D, Looney L. Development and assessment of a new quick quench stir caster design for the production of metal matrix composites. Journal of Materials Processing Technology. 2005;166:430-9.

[16] Kandemir S, Atkinson HV, Weston DP, Hainsworth SV. Thixoforming of A356/SiC and A356/TiB2 Nanocomposites Fabricated by a Combination of Green Compact Nanoparticle Incorporation and Ultrasonic Treatment of the Melted Compact. Metall and Mat Trans A. 2014.

[17] Isaikin AS, Chubarov VM, Trefilov BF, Silaev VA, Gorelov YA. Compatibility of carbon filaments with a carbide coating and an aluminum matrix. Met Sci Heat Treat. 1980;22:815-7.

[18] Surappa MK, Rohatgi PK. Preparation and properties of cast aluminium-ceramic particle composites. J Mater Sci. 1981;16:983-93.

[19] Bolling GF, Cissé J. A theory for the interaction of particles with a solidifying front. Journal of Crystal Growth. 1971;10:56-66.

[20] Agaliotis EM, Rosenberger MR, Ares AE, Schvezov CE. Influence of the Shape of the Particles in the Solidification of Composite Materials. Procedia Materials Science. 2012;1:58-63.

[21] Surappa MK, Rohatgi PK. Heat diffusivity criterion for the entrapment of particles by a moving solid-liquid interface. J Mater Sci. 1981;16:562-4.

[22] Khan MA, Rohatgi PK. A numerical study of thermal interaction of solidification fronts with spherical particles during solidification of metal-matrix composite materials. Composites Engineering. 1993;3:995-1006.

[23] Faugeras C, Faugeras B, Orlita M, Potemski M, Nair RR, Geim AK. Thermal Conductivity of Graphene in Corbino Membrane Geometry. ACS Nano. 2010;4:1889-92.

[24] Joshi RP, Neudeck PG, Fazi C. Analysis of the temperature dependent thermal conductivity of silicon carbide for high temperature applications. Journal of Applied Physics. 2000;88:265-9.

[25] Muñoz E, Lu J, Yakobson BI. Ballistic Thermal Conductance of Graphene Ribbons. Nano Letters. 2010;10:1652-6.

[26] Nye JF. Physical properties of crystals: their representation by tensors and matrices: Oxford university press; 1985.

[27] Frost HJ, Ashby MF. Deformation mechanism maps: the plasticity and creep of metals and ceramics. 1982.

[28] Bao W, Miao F, Chen Z, Zhang H, Jang W, Dames C, et al. Controlled ripple texturing of suspended graphene and ultrathin graphite membranes. Nat Nano. 2009;4:562-6.

[29] Liu X, Metcalf TH, Robinson JT, Houston BH, Scarpa F. Shear Modulus of Monolayer Graphene Prepared by Chemical Vapor Deposition. Nano Letters. 2012;12:1013-7.

[30] Lee C, Wei X, Kysar JW, Hone J. Measurement of the Elastic Properties and Intrinsic Strength of Monolayer Graphene. Science (New York, NY). 2008;321:385-8.

[31] Ramakrishnan N. An analytical study on strengthening of particulate reinforced metal matrix composites. Acta Materialia. 1996;44:69-77.

[32] MA M, CHAWLA K. Mechanical metallurgy: principles and applications. Prentice-Hall, Englewood Cliffs, New Jersey; 1984.

[33] Nardone VC, Prewo KM. On the strength of discontinuous silicon carbide reinforced aluminum composites. Scripta Metallurgica. 1986;20:43-8.

[34] Jiang T, Huang R, Zhu Y. Interfacial Sliding and Buckling of Monolayer Graphene on a Stretchable Substrate. Advanced Functional Materials. 2014;24:396-402.

[35] Carrara AS, Mcgarry FJ. Matrix and Interface Stresses in a Discontinuous Fiber Composite Model. Journal of Composite Materials. 1968;2:222-43.

[36] Nie JF. Effects of precipitate shape and orientation on dispersion strengthening in magnesium alloys. Scripta Materialia. 2003;48:1009-15.

[37] Zhang Z, Chen DL. Contribution of Orowan strengthening effect in particulate-reinforced metal matrix nanocomposites. Materials Science and Engineering: A. 2008;483–484:148-52.

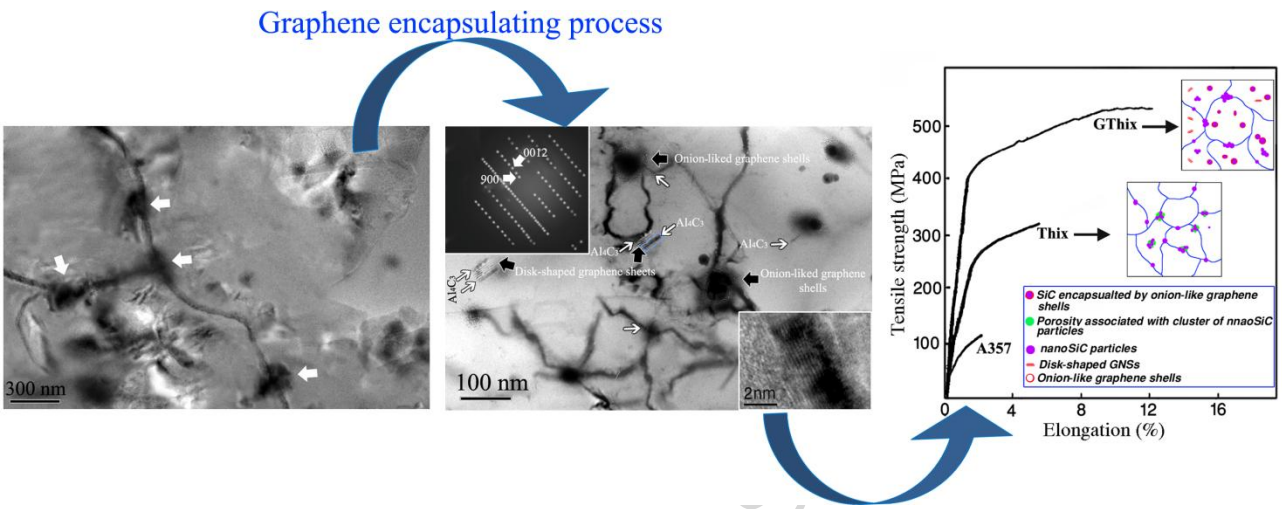

Graphical Abstract

Highlights
In this paper, we have shown:

- Production of Al-SiC composite reinforced with uniform distribution of SiC nanoparticles.
- The most important strengthening mechanisms of graphene sheets in aluminium matrix nanocomposites which can be used for other metal matrix composites.
- Enhanced tensile properties especially tensile elongation of aluminum based nanocomposites.